

# In-plane hyperbolic polariton tuners in terahertz and long-wave infrared regimes

**Wuchao Huang**

Sun Yat-sen University

**Thomas G. Folland**

Vanderbilt University

**Fengsheng Sun**

Sun Yat-sen University

**Zebo Zheng**

Guangdong Province Key Laboratory of Display Material and Technology, School of Electronics and Information Technology, Sun Yat-sen University

**Ningsheng Xu**

Guangdong Province Key Laboratory of Display Material and Technology, School of Electronics and Information Technology, Sun Yat-sen University

**Qiaoxia Xing**

Fudan University

**Jingyao Jiang**

Sun Yat-sen University

**Joshua Caldwell**

Vanderbilt University, Mechanical Engineering Department <https://orcid.org/0000-0003-0374-2168>

**Hugen Yan**

Fudan University <https://orcid.org/0000-0001-8423-6069>

**Huanjun Chen** (✉ [chenhj8@mail.sysu.edu.cn](mailto:chenhj8@mail.sysu.edu.cn))

Guangdong Province Key Laboratory of Display Material and Technology, Sun Yat-sen University  
<https://orcid.org/0000-0003-4699-009X>

**Shao-Zhi Deng**

Guangdong Province Key Laboratory of Display Material and Technology, School of Electronics and Information Technology, Sun Yat-sen University

---

## Article

## Keywords:

**Posted Date:** June 22nd, 2022

**DOI:** <https://doi.org/10.21203/rs.3.rs-1735989/v1>

**License:**   This work is licensed under a Creative Commons Attribution 4.0 International License.

[Read Full License](#)

---

# In-plane hyperbolic polariton tuners in terahertz and long-wave infrared regimes

Wuchao Huang<sup>1,†</sup>, Thomas G. Folland<sup>4,5,†</sup>, Fengsheng Sun<sup>1,†</sup>, Zebo Zheng<sup>1,†</sup>, Ningsheng Xu<sup>1,2</sup>, Qiaoxia Xing<sup>3</sup>, Jingyao Jiang<sup>1</sup>, Joshua D. Caldwell<sup>4,\*</sup>, Hugen Yan<sup>3,\*</sup>, Huanjun Chen<sup>1,\*</sup>, and Shaozhi Deng<sup>1,\*</sup>

<sup>1</sup>State Key Laboratory of Optoelectronic Materials and Technologies, Guangdong Province Key Laboratory of Display Material and Technology, School of Electronics and Information Technology, Sun Yat-sen University, Guangzhou 510275, China

<sup>2</sup>The Frontier Institute of Chip and System, Fudan University, Shanghai 200433, China

<sup>3</sup>State Key Laboratory of Surface Physics, Department of Physics, Key Laboratory of Micro and Nano-Photonic Structures (Ministry of Education), Fudan University, Shanghai 200433, China

<sup>4</sup>Department of Mechanical Engineering, Vanderbilt University, Nashville, TN 37235, USA

<sup>5</sup>Department of Physics and Astronomy, The University of Iowa, Iowa City, IA 52245, USA

\*e-mail: chenjh8@mail.sysu.edu.cn; stsdz@mail.sysu.edu.cn;  
Josh.caldwell@vanderbilt.edu; hgyan@fudan.edu.cn.

**Development of terahertz (THz) and long-wave infrared (LWIR) technologies is mainly bottlenecked by the limited intrinsic response of traditional materials. Hyperbolic phonon polaritons (HPhPs) of van der Waals semiconductors couple strongly with THz and LWIR radiation. However, the mismatch of photon-polariton momentum makes far-field excitation of HPhPs challenging. Here, we propose an In-Plane Hyperbolic Polariton Tuner and demonstrate a first device responding to direct far-field excitation and giving rise to a unique set of characteristic functions at far-field. Such a device is based on patterned surface directly written on van der Waals semiconductors; here  $\alpha$ -MoO<sub>3</sub>. The resonances are found to strongly rely on in-plane hyperbolic polariton of patterned  $\alpha$ -MoO<sub>3</sub>, exhibiting high quality factors up to 300, and to determine the characteristics of resultant tunable polarization and selection of the wavelength of reflection and transmission and regulation of output intensity. This is important to development of THz and LWIR miniaturized devices.**

The discovery of two-dimensional (2D) vdW crystals has opened new avenues for exploring novel functional materials and devices in the THz (30–3000  $\mu\text{m}$ ) and long-wave infrared (LWIR; 8–15  $\mu\text{m}$ ) spectral ranges<sup>1–11</sup>. The THz and LWIR technologies are of great significance for future photonic and optoelectronic applications, such as 5G/6G mobile networks<sup>12,13</sup>, night vision<sup>14</sup>, biomedical imaging and sensing<sup>15,16</sup>, thermal management<sup>17</sup>, and deep-space exploration<sup>18</sup>. However, their development is always limited by the scarcity of materials with strong and tunable intrinsic optical responses, in particular those used for devices in nanoscale and of room temperature operation.

In the past decades, much effort has been devoted to develop narrow band-gap

semiconductors (*e.g.*, mercury cadmium telluride and InSb) and quantum materials (*e.g.*, quantum wells/dots, super lattice)<sup>19–21</sup>, whose inter-band, intra-band, or inter-subband optical transitions are found in the LWIR and THz regimes. However, due to the relatively weak light-matter interaction, their optical responses are weak, and this is further affected by thermal noise. Thus their devices usually require cryogenic operation to suppress thermal noise, and the introduction of components such as antennas and/or light-absorbing layers to improve the electromagnetic absorption, the dimension of which will be out of the scale of tens of micrometers, not to mention the nanoscale. These will result in complex and large-volume architectures that are not favorable for nanodevices, even miniaturized and portable devices. Moreover, the broadband- and polarization-insensitive optical transitions of these materials also restrict their applications in spectrally and polarization-selective photonic and optoelectronic devices, which are particularly interesting in modern information society. Metamaterials and metasurfaces comprised of artificially designed metallic or dielectric unit cells are able to confine the THz and LWIR electromagnetic waves to enhance light-matter interactions, which therefore give rise to a variety of functional devices<sup>22–29</sup>. However, despite intense research efforts, in these spectral ranges the unit cells of many conventional metamaterial/metasurface often offer restricted confinement due to high losses<sup>22,30</sup>. These are not conducive to device integration, and will also increase device power consumption.

Recently, semiconducting vdW transition metal oxides, such as  $\alpha$ -MoO<sub>3</sub><sup>9–11</sup> and  $\alpha$ -V<sub>2</sub>O<sub>5</sub><sup>31</sup>, have been explored to exhibit phonon polaritons—quasiparticles formed by coupling of photons to phonons—with ultra-low-loss in the THz and LWIR regimes<sup>7,31–38</sup>. Due to the biaxial nature, in each Reststrahlen band bracketed by the longitudinal optical (LO) and transverse optical (TO) phonon frequencies, the real parts of the permittivities,  $\text{Re}(\epsilon)$ , along the three optical principal axes in these crystals are different, and there is always at least one negative component<sup>9–11,31,33,39</sup>. This means that the  $\alpha$ -MoO<sub>3</sub> and  $\alpha$ -V<sub>2</sub>O<sub>5</sub> can sustain natural in-plane HPhPs, enabling ultrahigh confinement and manipulation of the THz and LWIR radiation at nanoscale dimensions<sup>34–44</sup>.

However, so far the demonstration of utilizing the above exotic characteristics in a practical device is not given. The challenge lies in that one needs to compensate the large photon-polariton momentum mismatch for far-field excitation and far-field characterization of the HPhPs. In the previous studies the HPhPs of vdW crystals have been observed by near-field nano-imaging techniques<sup>9–11,31</sup>, relying on using a metallic nanotip to compensate the large momentum mismatch between free-space photons and polaritons. For most of practical device applications, direct excitation of the HPhPs from the far-field is necessary. Some earlier studies indicate that this may be possible by patterning the surface of vdW crystals, such as with graphene<sup>45–47</sup>, hexagonal boron nitride<sup>8,48,49</sup>, semi-metals<sup>50</sup>, and topological insulators<sup>51</sup>. However, far-field excitation and characterization of the tunable in-plane HPhPs in vdW crystals, especially in THz spectral regime, remain unexplored. This can be done if one has a surface of vdW crystal large enough so that patterns are made larger than the diffraction limit for these free-space wavelengths and thus, suitable for far-field spectroscopy.

In this article we demonstrate for the first time far-field excitation and far-field characterization of HPhPs in an In-Plane Hyperbolic Polariton Tuner that we propose. In such an in-plane tuner, patterns can be designed and directly written onto the semiconducting HPhP vdW crystals, here a vdW  $\alpha$ -MoO<sub>3</sub> flake with a centimeter lateral size. The THz and LWIR photons from far-field illuminating onto the tuner

will strongly couple with the phonons and give rise to polaritons, and the resultant effects are characterized by a spectroscopy at far-field. We find that an in-plane tuner is a unique device, and that it acts not only with functions of grating but also a polarizer and filter in the LWIR and THz regimes, and have distinctive features including high-Q (300) resonance and extinction ratios up to 6.5 dB at a deep sub-wavelength thickness of 200 nm, which is impossible without HPhPs. This could potentially be significantly improved through the optimization of the geometries and substrates.

### **Fabrication of in-plane hyperbolic polariton tuner and far-field excitation of HPhPs**

An in-plane tuner will have structured surface written with desirable patterns. In this study, the in-plane tuner consists of simple one-dimensional periodic ribbon patterns (1D-PRPs) directly formed on a vdW  $\alpha$ -MoO<sub>3</sub> flake using electron-beam lithography (EBL). They have widths ( $w$ ) and skew angles ( $\theta$ ), which is defined by the angle between the long-axis ribbon direction and [001] crystallographic axis of vdW  $\alpha$ -MoO<sub>3</sub> (Fig. 1a). The ribbon period ( $\Lambda$ ) is set as  $2w$ . Both of  $w$  and  $\Lambda$  are much smaller than the excitation wavelength. As such, we synthesized a 120 nm-thick  $\alpha$ -MoO<sub>3</sub> crystal with a largest lateral size larger than 1-cm (Fig. 1b and Fig. S1 in Supplementary Information, and see Methods for details), which guarantees the fabrication, characterization, and comparison of different tuners on the same flake (Fig. 1c and Fig. S2 in Supplementary Information). The basal plane of the as-grown  $\alpha$ -MoO<sub>3</sub> is (010) plane, with the two orthogonal directions corresponding to [100] and [001] crystallographic axes, respectively<sup>9–11</sup>. In our study, these two axes are defined as the  $x$ - and  $y$ -axes, respectively (Fig. 1a), which are identified experimentally using micro-Raman spectroscopy (Fig. S1b – d in Supplementary Information). A broadband THz and LWIR light illuminates the tuner and the responsive optical measurements at far-field was carried out using a polarized Fourier transform infrared (FTIR) micro-spectroscopy (Fig. 1a). This technique has been widely employed to determine the polaritonic properties of various 2D crystals due to its ability for spectroscopic characterization over a broad spectral range, with a high collection efficiency, and over a large sample area (see Methods for details)<sup>39,52,53</sup>.

In vdW  $\alpha$ -MoO<sub>3</sub> crystal, in the spectral regimes 230 – 400 cm<sup>-1</sup> (THz) and 545 – 1010 cm<sup>-1</sup> (LWIR) there are a series of Reststrahlen bands where the  $\text{Re}(\epsilon)$  along one of the three crystallographic axes, *i.e.*, [100], [001], and [010], is negative (Fig. S3 in Supplementary Information), while at least one is positive. This makes  $\alpha$ -MoO<sub>3</sub> a natural hyperbolic medium capable of supporting HPhPs. We first characterized the far-field reflection of the homogeneous pristine  $\alpha$ -MoO<sub>3</sub>, which is calculated as  $R/R_0 - 1$ , with  $R$  and  $R_0$  the reflectance of the light from the surfaces of sample and bare substrate (see Methods). For incident light polarized along the [001] and [100] directions, the reflectance spectra show distinct peaks at 550 and 820 cm<sup>-1</sup> (Fig. 1d), which correspond to IR-active TO phonon modes along [001] ( $\omega_{\text{TO}}^{001}$ ) and [100] axes ( $\omega_{\text{TO}}^{100}$ ), respectively. Both of the spectra exhibit small valleys at 1004 cm<sup>-1</sup>. These valleys are very close to the frequency of LO phonon mode along [010] axis ( $z$ -axis,  $\omega_{\text{LO}}^{010}$ ) where the permittivity diminishes. For a 120 nm-thick  $\alpha$ -MoO<sub>3</sub> flake, leaky modes (Berreman modes) can be excited near this epsilon-near-zero (ENZ) region and then give rise to the two valleys on the reflectance spectra<sup>54–56</sup>. These narrow leaky modes can further interfere with the broad reflection background and generate asymmetric Fano lineshapes (see Note S1 and Fig. S4 in Supplementary Information).

However, no evident spectral peaks corresponding to HPhPs are observed in the rest of the spectral range. This is due to the large wavevector mismatch between free-space photons ( $k_0$ ) and polaritons ( $q_{\text{PhPs}}$ ), which prevents the coupling of electromagnetic fields to HPhPs.

A tuner comprised of 1D-PRPs (Fig. 1c and Fig. S2 in Supplementary Information) is able to overcome the large momentum mismatch. This is because the 1D-PRPs can diffract the incident light into evanescent waves whose wavevectors are perpendicular to the ribbon long axis and differ by a reciprocal lattice momentum  $G = m\pi/w$ , with  $m$  an integer not equal to 0. The evanescent waves can then hybridize with the phonons and form PhPs propagating perpendicular to the 1D-PRP. Such a process therefore enables the far-field excitation of the PhPs. Once the polaritons are stimulated, they will propagate along the ribbons and form standing-wave resonances due to the multiple reflections from the ribbon edges. The coupled light fields will be dissipated by the lattice vibrations or radiated back to the free space, as manifested by resonance peaks and valleys in the corresponding reflectance and transmission spectra, respectively.

For a typical 1D-PRP with  $w = 800$  nm and orientated along the [001] axis (sample with skew angle  $\theta = 0^\circ$  shown in Fig. 1d), HPhPs in Reststrahlen Band 2 (820 to 972  $\text{cm}^{-1}$ , where  $\text{Re}(\varepsilon_x) < 0$  and  $\text{Re}(\varepsilon_y), \text{Re}(\varepsilon_z) > 0$ ) will be excited upon illumination polarized along the [100] axis. This will lead to a strong reflectance peak at 874  $\text{cm}^{-1}$ , as shown in Fig. 1e. The small bump at 820  $\text{cm}^{-1}$  originates from the intrinsic  $\omega_{\text{TO}}^{100}$ . No resonance peaks are observed when the polarization is switched to [001] direction. In contrast, for 1D-PRP orientated along the [100] axis (sample with  $\theta = 90^\circ$  shown in Fig. 1c), a clear peak at 689  $\text{cm}^{-1}$  is identified (Fig. 1f), suggesting the launching of HPhPs in Reststrahlen Band 1 (545 to 851  $\text{cm}^{-1}$ , where  $\text{Re}(\varepsilon_y) < 0$  and  $\text{Re}(\varepsilon_x), \text{Re}(\varepsilon_z) > 0$ ). For polarization along the [100] axis, only the  $\omega_{\text{TO}}^{100}$  peak appears. The excitation of HPhPs in both Bands 1 and 2 using these two types of 1D-PRPs can be further confirmed by simulating the near-field distributions they support. The simulated field distributions at  $\omega = 874$  and 689  $\text{cm}^{-1}$  clearly reveal that polaritonic rays with “zig-zag” patterns propagate inside the ribbons (Fig. S5a, S5b, and Note S2 in Supplementary Information). These are typical fingerprints of HPhP waveguide modes, such as those observed in hBN nanostructures<sup>57</sup> and biaxial  $\alpha$ -MoO<sub>3</sub> flakes<sup>58</sup>.

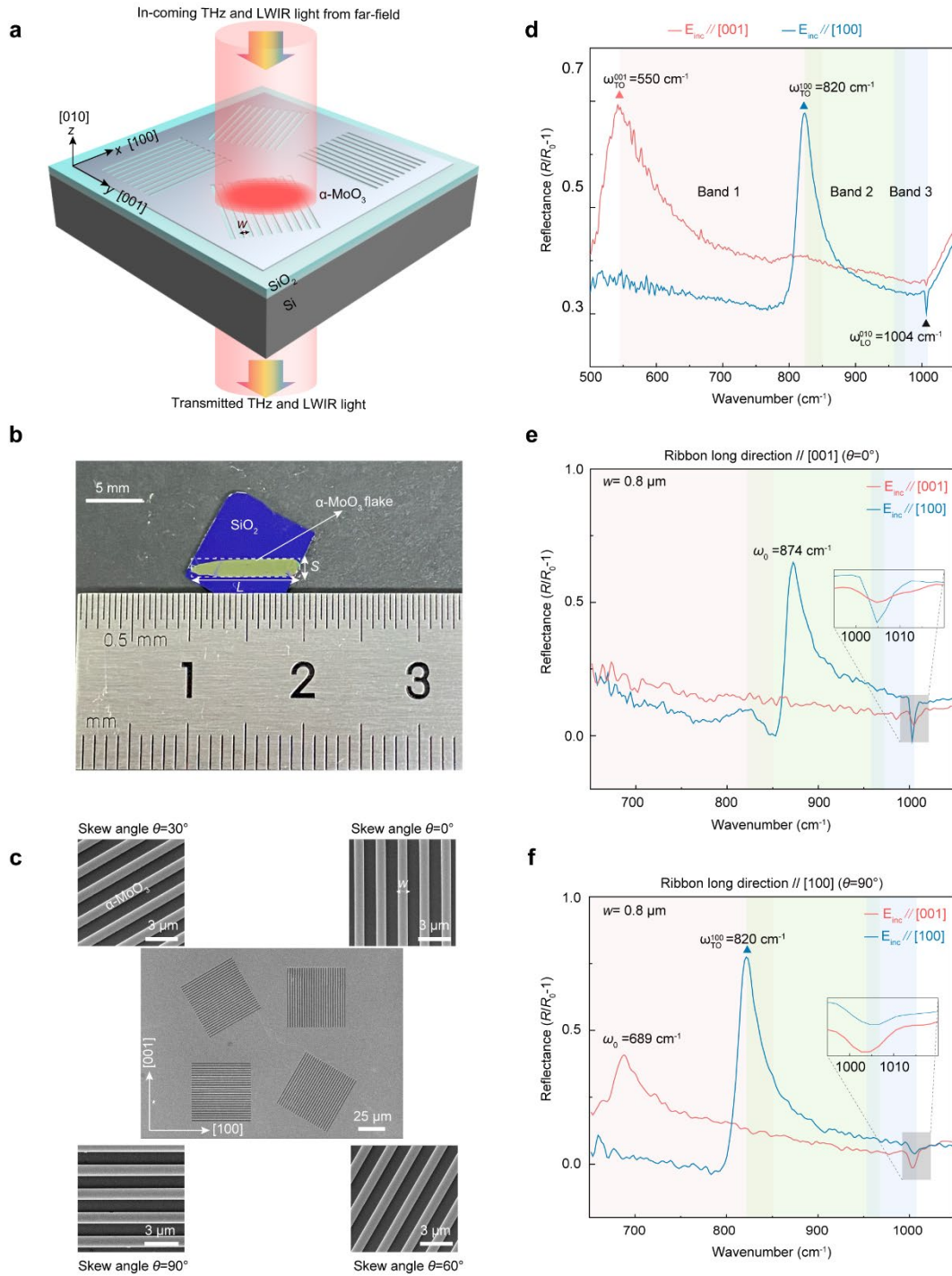


**Fig. 1 | Far-field excitations of HPhPs in in-plane hyperbolic polariton tuners. a**, Schemes of the tuners comprised of vdW  $\alpha\text{-MoO}_3$  periodic ribbon patterns and FTIR measurements. **b**, Photograph of a typical  $\alpha\text{-MoO}_3$  flake grown on silicon substrate with a 300-nm oxide layer. The largest lateral length of the flake is 1 cm. **c**, Scanning electron microscopy image of periodic ribbon patterns with a fixed  $w = 800$  nm and different skew angles  $\theta$  of  $0^\circ$ ,  $30^\circ$ ,  $60^\circ$ , and  $90^\circ$ . **d**, Polarized reflectance spectra of the pristine  $\alpha\text{-MoO}_3$  thin flake shown in (b). The electric fields of the incident light,  $E_{\text{inc}}$ , are along  $[001]$  (red curve) and  $[100]$  (blue curve) crystallographic directions, respectively. **e**, **f**, Experimental polarized reflectance spectra of one-dimensional periodic tuner patterns with  $\theta = 0^\circ$  (e) and  $90^\circ$  (f). The polarization of the incident

light is paralleled to [001] (red curves) and [100] (blue curves) directions, respectively. Insets: enlarged reflectance spectra in the range of 995 to 1020  $\text{cm}^{-1}$ .

Notably, in the two 1D-PRPs two valleys with narrow linewidths appear around 1000  $\text{cm}^{-1}$  for both polarization conditions. These valleys are spectrally close, but occur with different amplitudes, with the spectral valleys deeper when the incident light is polarized perpendicular to the ribbon. In addition, as discussed below, the deeper valleys shift when  $w$  and  $\theta$  change. Therefore, they are ascribed to HPhP resonances in Reststrahlen Band 3 (958 to 1010  $\text{cm}^{-1}$ , where  $\text{Re}(\epsilon_z) < 0$  and  $\text{Re}(\epsilon_x), \text{Re}(\epsilon_y) > 0$ ). This is also corroborated by the corresponding near-field distributions showing polaritonic rays with zig-zag shapes (Fig. S5c and d in Supplementary Information). Due to their narrow linewidths, Fano interference will occur between the background reflectance and the HPhP resonances, giving rise to these valley features (see Note S2 and Fig. S3 in Supplementary Information). The shallower valleys are contributed by the aforementioned ENZ condition that occurs near the  $\omega_{\text{LO}}^{010}$  (Fig. 1d). These results are consistent with polariton propagation in the basal plane of an  $\alpha\text{-MoO}_3$  flake: the HPhPs in Band 1 and 2 are of in-plane hyperbolicity, which cannot propagate along [100] and [001] directions, respectively<sup>11</sup>. In contrast, the dispersion of HPhPs in Band 3 are elliptical, which therefore allows them to propagate along both of the two orthogonal crystallographic directions<sup>11</sup>.

### **Tuning the HPhP resonance with tuner patterns of different structural parameters**

The above results clearly prove that the HPhPs supported by  $\alpha\text{-MoO}_3$ , which previously were only accessed using near-field nano-imaging<sup>9-11,33,34</sup>, are able to be excited from far-field using the 1D-PRPs. To demonstrate the tunability of HPhPs in this material, we measured the reflectance spectra of 1D-PRPs with different  $w$  ranging from 100 to 2000 nm. All spectra were collected with the incident light polarized perpendicular to the ribbon long axis. For 1D-PRPs parallel to the [100] direction, both of the HPhP resonances corresponding to Band 1 (peaks) and 3 (valleys) can be excited (Fig. 2a). Notably, when  $w$  increases from 600 to 2000 nm, the resonance in Band 1 clearly redshifts from 746 to 613  $\text{cm}^{-1}$ , whereas a reverse trend appears for the modes in Band 3, where the resonances blueshift from 998 to 1005  $\text{cm}^{-1}$ . Similar spectral evolution with changing  $w$  can be observed for 1D-PRPs along the [001] direction (Fig. 2b), where PhP resonances in Band 2 and 3 are excited. Additionally, the variation of resonance frequency in Band 3 with  $w$  is different for these two ribbon orientations (Fig. S6 in Supplementary Information).

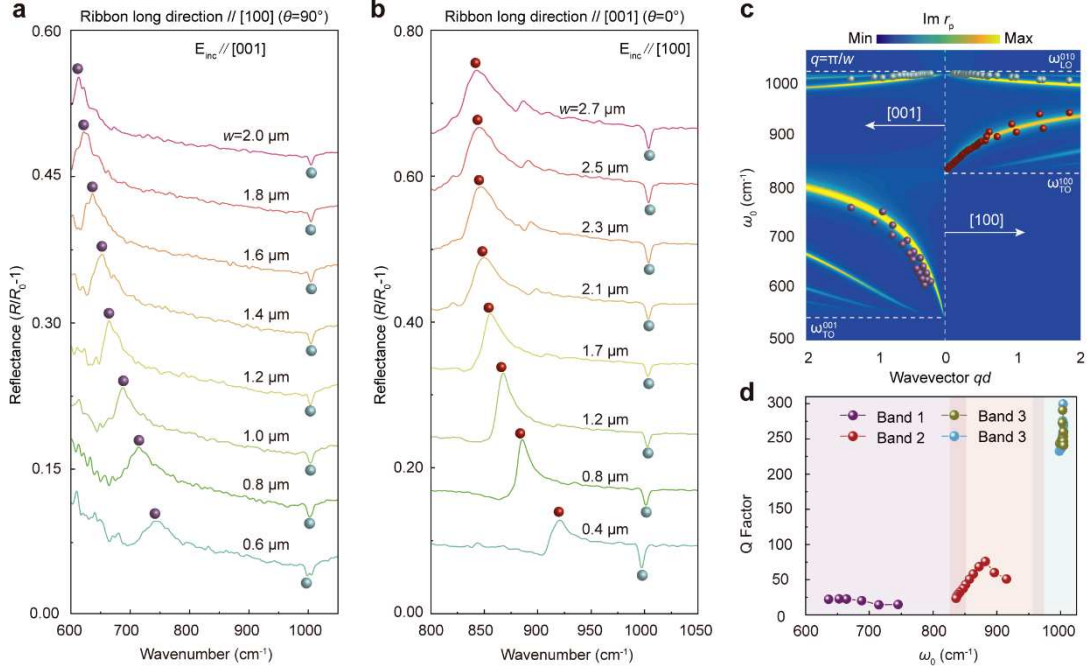


**Fig. 2 | Tuning HPhP resonances with tuner patterns of different ribbon widths. a, b,** Experimentally measured reflectance spectra of tuners with different ribbon widths  $w$ , showing the large resonance shift in the reflectance spectra by changing  $w$  within one micrometer. The ribbon long axes are paralleled to the [100] (a) and [001] (b) crystallographic directions, respectively. The colored spheres indicate the resonance frequencies. **c,** Comparison of the theoretically derived (false color plot) and experimental (color spheres) HPhP dispersion relations, showing the exact matching between the two results. The color spheres are extracted from reflectance spectra at different  $w$ . The false color plot represents the calculated  $\text{Im}r_p(q_{\text{PhPs}}, \omega)$  of the air/ $\alpha$ -MoO<sub>3</sub>/SiO<sub>2</sub>/Si multilayered structure. The polariton wavevector is normalized by the thickness of the  $\alpha$ -MoO<sub>3</sub> flake. **d,** Dependence of Q-factor on  $\omega_{\text{res}}$  extracted from the reflectance spectra shown in (a) and (b). In Band 1 and 3, the Q-factors respectively decrease and increase monotonically as the  $\omega_0$  increase, whereas the non-monotonically trend has been observed in Band 2. A Q-factor as high as 300 can be obtained for resonance in Band 3.

The evolution of the HPhP resonances with changing  $w$  can be understood by considering that each  $w$  corresponds to an in-plane polariton wavevector of  $q_{\text{PhPs}} = k_0 \sin \alpha \mp G \approx \mp G = \mp \frac{m\pi}{w}$ , where  $\alpha$  is the incident angle<sup>59</sup>. When  $w$  changes the resonance peak will scale according to the in-plane polariton dispersion relations,  $\omega(q_{\text{PhPs}})$ . This can be readily seen by calculating the  $\omega(q_{\text{PhPs}})$  along the [100] and [001] directions, which is visualized as the 2D false color plot of the imaginary part of the complex reflectivity  $\text{Im}r_p(q_{\text{PhPs}}, \omega)$  (see Note S3 in Supplementary Information for details on calculation of  $\text{Im}r_p$ ). The PhP resonance frequencies obtained from the spectra shown in Fig. 2a and b are then overlaid onto the same plot by using  $q_{\text{PhPs}} = m\pi/w$ . Excellent agreement is obtained between the experimental measurements and calculated lowest-order ( $m = 1$ ) HPhP branches for all the three bands (Fig. 2c). Such an agreement further validates that the highly anisotropic HPhPs in the  $\alpha$ -MoO<sub>3</sub> flake are directly excited from the far-field with the help of the in-plane hyperbolic polariton tuners.

The far-field reflectance spectra allow for evaluating the Q-factor of the HPhP resonance, which is defined as  $Q = \frac{\omega_0}{\Gamma}$ , with  $\omega_0$  and  $\Gamma$  the frequency and linewidth of a specific resonance<sup>8</sup> (see details in Note S1 in Supplementary Information for extraction of the Q-factors). For HPhP resonances in Band 1 and 3, their Q-factors respectively decrease and increase monotonically against  $\omega_0$  (Fig. 2d). This is because when  $\omega_0$  increases, the PhP resonance in Band 1 shifts closer to the  $\omega_{\text{TO}}^{100}$  (820 cm<sup>-1</sup>), while the resonance in Band 3 shifts away from the TO phonon mode along [010] axis at 958 cm<sup>-1</sup> ( $\omega_{\text{TO}}^{010}$ )<sup>11,39</sup>. Thus the polariton dissipation by lattice absorption will be strengthened (suppressed) for Band 1 (Band 3), giving rise to a larger (smaller)  $\Gamma$ . The non-monotonic behavior of the Q-factor for the HPhP resonance observed in Band 2 can be understood by considering that in addition to  $\omega_{\text{TO}}^{100}$ , there is another LO phonon mode along the [100] axis at 972 cm<sup>-1</sup> ( $\omega_{\text{LO}}^{100}$ )<sup>11,39</sup>. Leaky-mode absorption induced by ENZ condition also occurs near the  $\omega_{\text{LO}}^{100}$ . Therefore, the Q-factor first increases as  $\omega_0$  is farther from the  $\omega_{\text{TO}}^{100}$ , and then decreases gradually approaching the  $\omega_{\text{LO}}^{100}$ . It is noted that the Q-factors observed in the Band 1, 2, and 3 are 15–25, 25–100, and 200–300, respectively. Most of these values are higher than those observed in graphene nano-gratings with similar resonance frequencies<sup>46,47,52</sup>. In particular, the Q-factor of the Band 3 resonance can be as high as 300, which is on par with the highest observed in hBN nanoresonators (360)<sup>60</sup>. Such high Q-factors, coupled with the small modal volumes and footprint of the 1D-PRPs, indicate that the  $\alpha$ -MoO<sub>3</sub> tuners offer important application potential for high-efficiency compact photonic devices and components, as demonstrated below.

### Tuning the HPhPs with periodic tuner patterns of different skew angles

The in-plane HPhP dispersions of the  $\alpha$ -MoO<sub>3</sub> are highly anisotropic<sup>10,11</sup>. This offers unique tunability of the HPhP resonances by changing the 1D-PRP orientations, which cannot be realized in vdw crystals with isotropic in-plane dispersions such as hBN and graphene. As such, 1D-PRPs with fixed  $w$  (480 nm), but different  $\theta$  were fabricated (Fig. 3a and Fig. 1c). Each pattern can provide polariton momenta of  $q_{\text{PhPs}} = \pi/w$ , with the direction perpendicular to the ribbon long axis. In this way, when the ribbon is rotated away from the [001] axis, HPhPs with wavevectors of different orientations within the basal plane can be excited, giving rise to HPhP resonances that are strongly dependent on the  $\theta$ . Specifically, HPhP resonances in Band 2 and 3 can be observed for  $\theta = 0^\circ$ , and all of HPhP resonances in Band 1, 2, and 3 appear when  $\theta$  is increased (Fig. 3b). For  $\theta = 90^\circ$ , the resonance in Band 2 merges with the  $\omega_{\text{TO}}^{100}$ . In addition, the resonances in Band 1 and 2 are highly sensitive to  $\theta$ , while that in Band 3 shifts slowly against  $\theta$  (Fig. 3b). This can be ascribed to the distinct in-plane polariton dispersions of the three bands. Specifically, the in-plane isofrequency contour (IFC) of HPhPs in Band 3 is an ellipse, where the polariton dispersion differs moderately along different directions in the basal plane. However, the IFCs in Band 1 and 2 are hyperbola, making their polariton dispersions highly dispersive with  $\theta$ . These angle-dependent behaviors can be seen more clearly by plotting the dependence of resonance frequencies in the three bands on the skew angle (Fig. 3c), which agree well with the calculated  $\text{Im}r_p(q_{\text{PhPs}}, \omega)$ .

The HPhP dispersion relations at each skew angle can be obtained by measuring the reflectance spectra from 1D-PRPs with different  $w$  ( $q_{\text{PhPs}}$ ) at a specific  $\theta$  (Fig. S7

in Supplementary Information), whereby the in-plane polariton IFCs at different energies can be re-constructed and visualized. Clearly, the HPhP resonances in Band 1 and 2 depict IFCs of open hyperbolic shapes (Fig. 3d and e), while those in Band 3 correspond to an IFC of a closed ellipse (Fig. 3f). Moreover, at higher frequencies in Band 1 (Band 2), the opening-angles of the hyperbolic sectors become smaller and the hyperbola bends toward the [001] ([100]) direction (Fig. 3d and e). All the experimental points can be fit well by the calculated  $\text{Im}r_p$  (pseudo-colored plots shown in Fig. 3d–f and Fig. S7 in Supplementary Information). These results provide further direct evidence for far-field excitation and modulation of the hyperbolic HPhPs in the  $\alpha$ -MoO<sub>3</sub> flake.

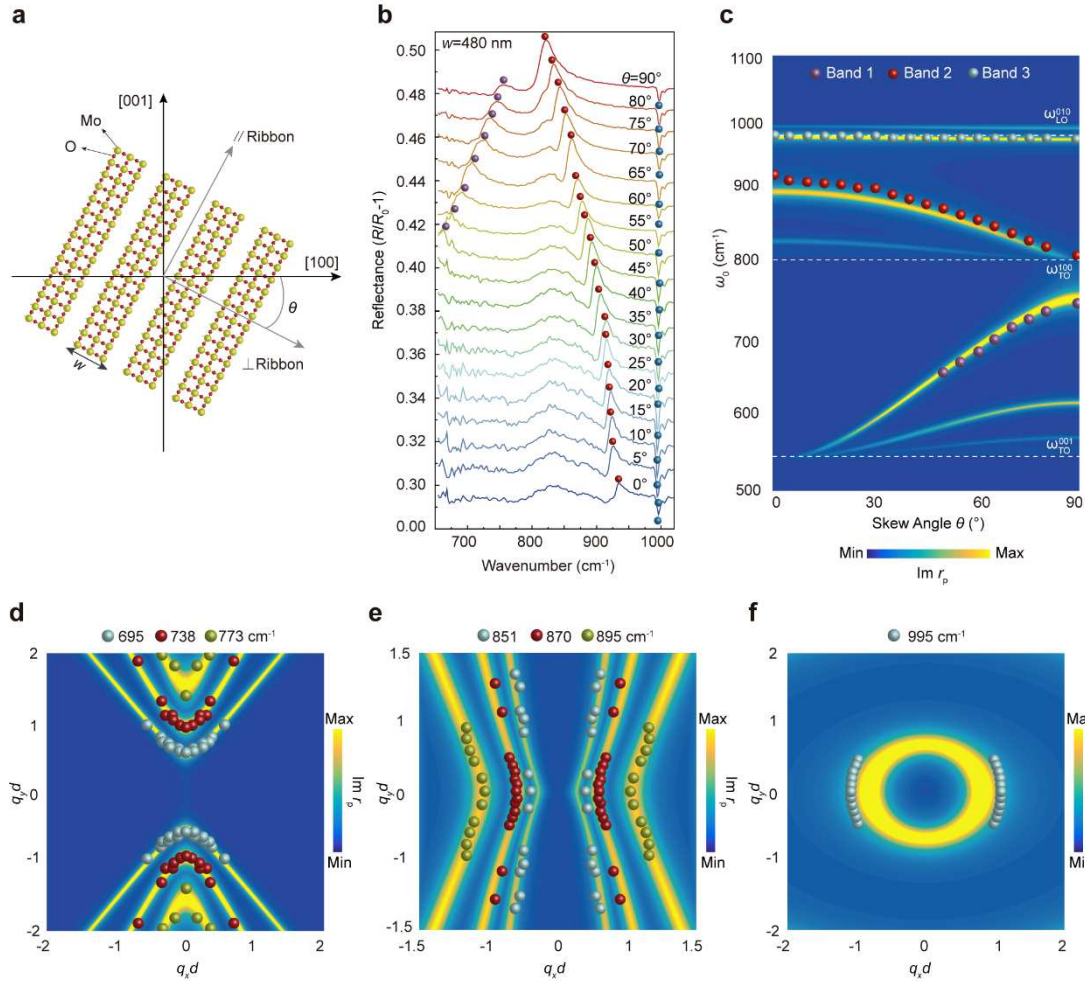


**Fig. 3 | Tuning the HPhPs with periodic tuner patterns of different skew angles. a,** Schematic showing 1D periodic tuner patterns with a skew angle  $\theta$ . **b,** Experimental reflectance spectra of 1D periodic tuner patterns with different  $\theta$ , showing that when  $\theta$  increases, the resonance in Band 1 clearly blueshifts, whereas a reverse trend appears in Band 2, and a slow variation of the resonance occurs in Band 3. The widths of the ribbons are kept at  $w = 480$  nm. The colored spheres depict the resonance frequencies. **c,** HPhPs resonance frequency,  $\omega_{\text{res}}$ , as a function of  $\theta$ , showing the consistency between the calculation and experimental results. The false color plot represents the calculated  $\text{Im}r_p(\theta, \omega_{\text{res}})$  of the air/ $\alpha$ -MoO<sub>3</sub>/SiO<sub>2</sub>/Si multilayered structure. The colored spheres correspond to the experimental resonance peaks extracted from the curves in (b). **d–f,** Polariton IFCs at different frequencies in Band 1 (d), Band 2 (e), and Band 3 (f), respectively, showing clear hyperbola for Band 1 and 2, while an ellipse for Band 3. The false color plots represent the  $\text{Im}r_p(\omega, q_{\text{PhPsx}}, q_{\text{PhPsy}})$ . The colored spheres in the

first quadrant represent the experimental resonance peaks at  $695.0 \pm 0.9$ ,  $738.0 \pm 0.8$ ,  $773.0 \pm 0.7$ ,  $851.0 \pm 0.9$ ,  $870.0 \pm 0.9$ , and  $895.0 \pm 0.9$   $\text{cm}^{-1}$ . Spheres in other quadrants are duplicated according to the symmetry of the measurement scheme and the  $\alpha\text{-MoO}_3$  crystal. The wavevectors in (c–f) are normalized by the thickness of the  $\alpha\text{-MoO}_3$  flake.

### Far-field excitation of tunable THz HPhPs using periodic tuner patterns

The  $\alpha\text{-MoO}_3$  flake can also support nanoscale-confined HPhPs in the THz domain from 260–400  $\text{cm}^{-1}$  (8–12 THz) which, however, have only been probed using the near-field nano-imaging technique<sup>33</sup>. To demonstrate the far-field excitation and tuning of the THz HPhPs, we fabricated 1D-PRPs of different  $w$  and  $\theta$  and characterized their spectral responses. Due to the relatively low signal-to-noise ratio of the bolometer in THz domain, transmission spectra were recorded, which is defined as  $T/T_0$ , with  $T$  and  $T_0$  the transmittance of the light through the sample and bare substrate (Methods). For 1D-PRPs with long axes parallel with [100] and [001] directions, we observed that resonance valleys associated with polariton wavevectors along the [001] (HPhP<sub>[001]</sub>, left panel) and [100] (HPhP<sub>[100]</sub>, right panel) direction can be excited in the spectral range of 270–330  $\text{cm}^{-1}$  and 350–400  $\text{cm}^{-1}$ , respectively (Fig. 4a). The tunability of these two resonances is clearly demonstrated by their redshifting behaviors with increasing  $w$ . The polariton dispersion relations were then obtained by extracting the resonance frequencies at different  $w$ . The analytical dispersions were derived using the dielectric tensor reported in Ref. 33 and are in good agreement with the experiment measurements (Fig. 4b, Note S4 in Supplementary Information). The Q-factors of the two types of resonances can be evaluated according to the transmittance spectra shown in Fig. 4a, which both increase with increasing the resonance frequency (Fig. 4d). The available Q-factors are in the range of 15–25 (HPhP<sub>[001]</sub>) and 23–47 (HPhP<sub>[100]</sub>) respectively, which surpass that of graphene plasmon resonance in the THz regime<sup>45</sup>.

The HPhP resonances are also strongly dependent on the skew angle of the 1D tuner patterns. By sweeping the  $\theta$  from 0° to 90° (ribbon long axis rotating from [001] to [100] direction), the HPhP<sub>[001]</sub> and HPhP<sub>[100]</sub> resonances shift monotonically to higher and lower frequencies, respectively (Fig. 4c). Moreover, with the experimental data shown in Fig. 4b and c, the in-plane IFC of the HPhP<sub>[001]</sub> can readily be drawn to exhibit a clear hyperbola opening towards the [001] axis (Fig. S8 in Supplementary Information). These results corroborate the excitation of HPhP resonances in THz Reststrahlen Band 1 (HPhP<sub>[001]</sub>) and 3 (HPhP<sub>[100]</sub>), which are consistent with the previous nano-imaging results<sup>33</sup>.

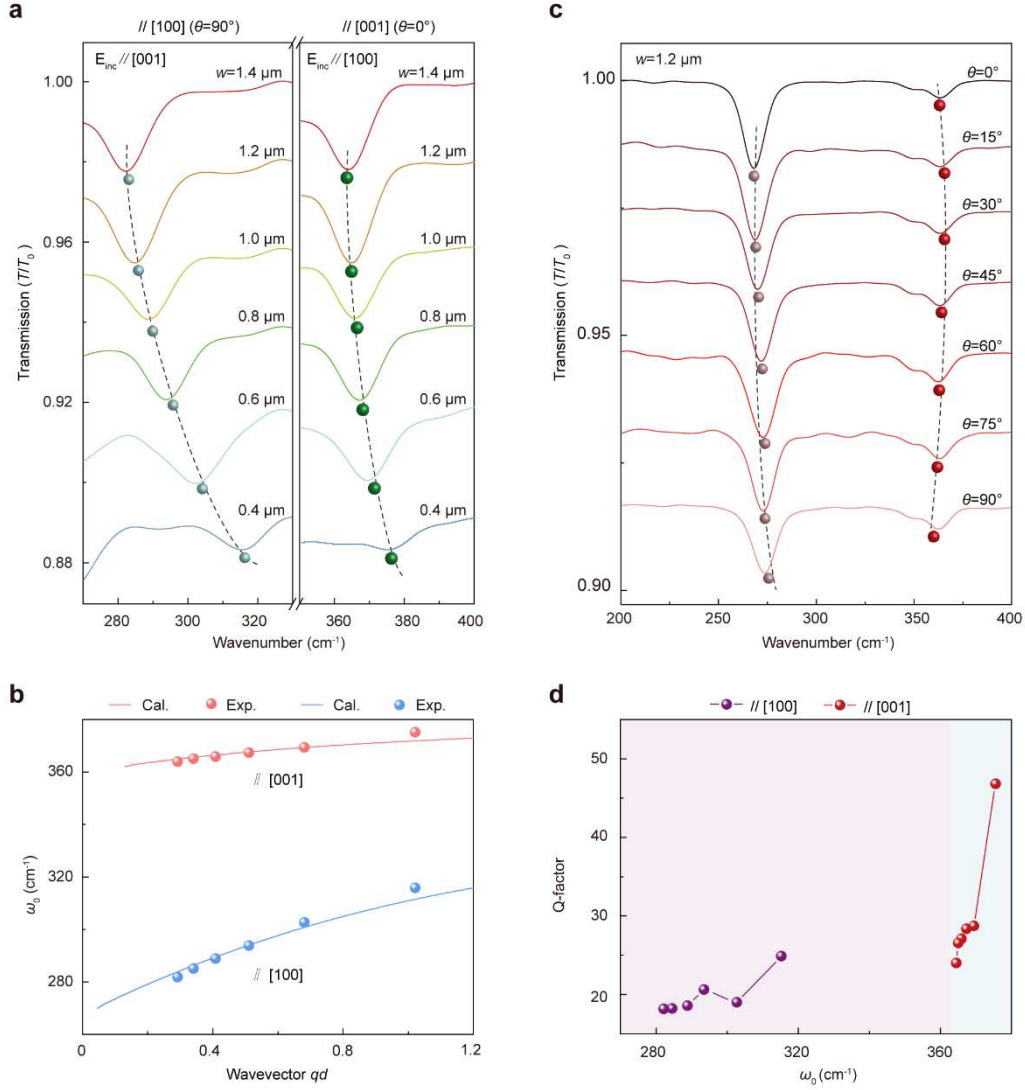


**Fig. 4 | Far-field excitations of tunable THz HPhPs in  $\alpha$ -MoO<sub>3</sub> one-dimensional periodic tuner patterns.** **a**, Experimental transmittance spectra of tuner patterns with different ribbon widths, showing redshifting behaviors of the two resonance valleys with changing  $w$ . The long axes of the ribbons are paralleled to the [100] (left panel) and [001] (right panel) crystallographic directions, respectively. The colored spheres indicate the resonance frequencies. **b**, HPhP dispersion relations in the THz regime, showing the consistence between the results of calculation and experiment. The wavevector is normalized by the thickness of the  $\alpha$ -MoO<sub>3</sub> flake. The colored solid lines are the calculated results according to the analytical dispersion relations of HPhPs propagating in the  $\alpha$ -MoO<sub>3</sub> flake. The colored spheres show the experimental results extracted from (a). **c**, Experimental transmittance spectra of tuner patterns with different  $\theta$ , showing that as  $\theta$  increase, the HPhP<sub>[001]</sub> and HPhP<sub>[100]</sub> resonances shift monotonically to higher and lower frequencies, respectively. The ribbon widths are fixed as  $w = 1200 \text{ nm}$ . The colored spheres indicate the resonance frequencies. **d**, Dependence of Q-factor on  $\omega_{\text{res}}$ , showing that in Band 1 and 3, the Q-factors increase monotonically as the  $\omega_0$  increases. The solid spheres are extracted from the transmittance spectra in (a). The solid lines are guide for eyes.

### Tunable LWIR and THz polarization notch filters

A PNF is a unique optical component that combines a polarizer and a narrow

band-rejection filter together into a single component, which is able to block a monochromatic laser with a given linear polarization, while passing light of all polarization states at wavelengths adjacent to the laser line. Such a filter has broad application prospects in laser spectroscopy and optical communications, but the commercial products are rare, and especially, there is no commercial PNF in the LWIR and THz ranges. The salient high-Q (Fig. 2d and Fig. 4d) and polarization-sensitive (Fig. 1e and f)  $\alpha$ -MoO<sub>3</sub> tuners established above provide opportunities for developing tunable PNFs<sup>61</sup>. As such, we constructed PNFs using 1D-PRPs with long axes along [001] and [100] axes, respectively. For typical 1D-PRPs with  $w = 1000$  nm, their extinction spectra in LWIR (Fig. 5a) and THz (Fig. 5c) regimes are strongly polarization-dependent. Specifically, the HPhP resonances only appear when the excitation polarization is perpendicular to the ribbon long axis. This can be seen more clearly by plotting the extinction at the corresponding resonance peaks, *i.e.*  $650\text{ cm}^{-1}/270\text{ cm}^{-1}$  and  $869\text{ cm}^{-1}/362\text{ cm}^{-1}$ , against light polarization for ribbons parallel to [100] and [001] directions, respectively (Fig. 5b and d). The performance of a PNF for blocking a monochromatic light source can be evaluated by two parameters: the polarization extinction ratio and bandwidth. Specifically, the polarization extinction ratio is defined as  $10\log(T_0/T)$ , with  $T_0$  and  $T$  the transmittance of light polarized along and perpendicular to the ribbon long axis at the resonance frequency. The bandwidth can be calculated according to the full width at half maximum (FWHM) of a specific resonance. Accordingly, for the PNFs with resonances at 650, 869, 270, and 362  $\text{cm}^{-1}$ , corresponding extinction ratios (bandwidth) are 3.4 dB (41.5  $\text{cm}^{-1}$ ), 5.5 dB (26.5  $\text{cm}^{-1}$ ), 4.5 dB (23.4  $\text{cm}^{-1}$ ) and 3.7 dB (24.5  $\text{cm}^{-1}$ ), respectively. In particular, the bandwidths of the PNFs are comparable to many of the commercial narrow-band-pass filters in similar spectral regimes, which are usually polarization insensitive, (Fig. S11 in Supporting Information), while the thicknesses of the PNFs (200 nm) are much smaller than those of these commercial components ( $\sim 1$  mm). More importantly, using 1D-PRPs with different  $w$ , the operational frequency, polarization extinction ratio, and FWHM of the PNF can be engineered continuously (Fig. S9 and Fig. S10 in the Supplementary Information). The maximum peak extinction can reach 6.5 dB and the smallest FWHM can be as narrow as 17  $\text{cm}^{-1}$ .

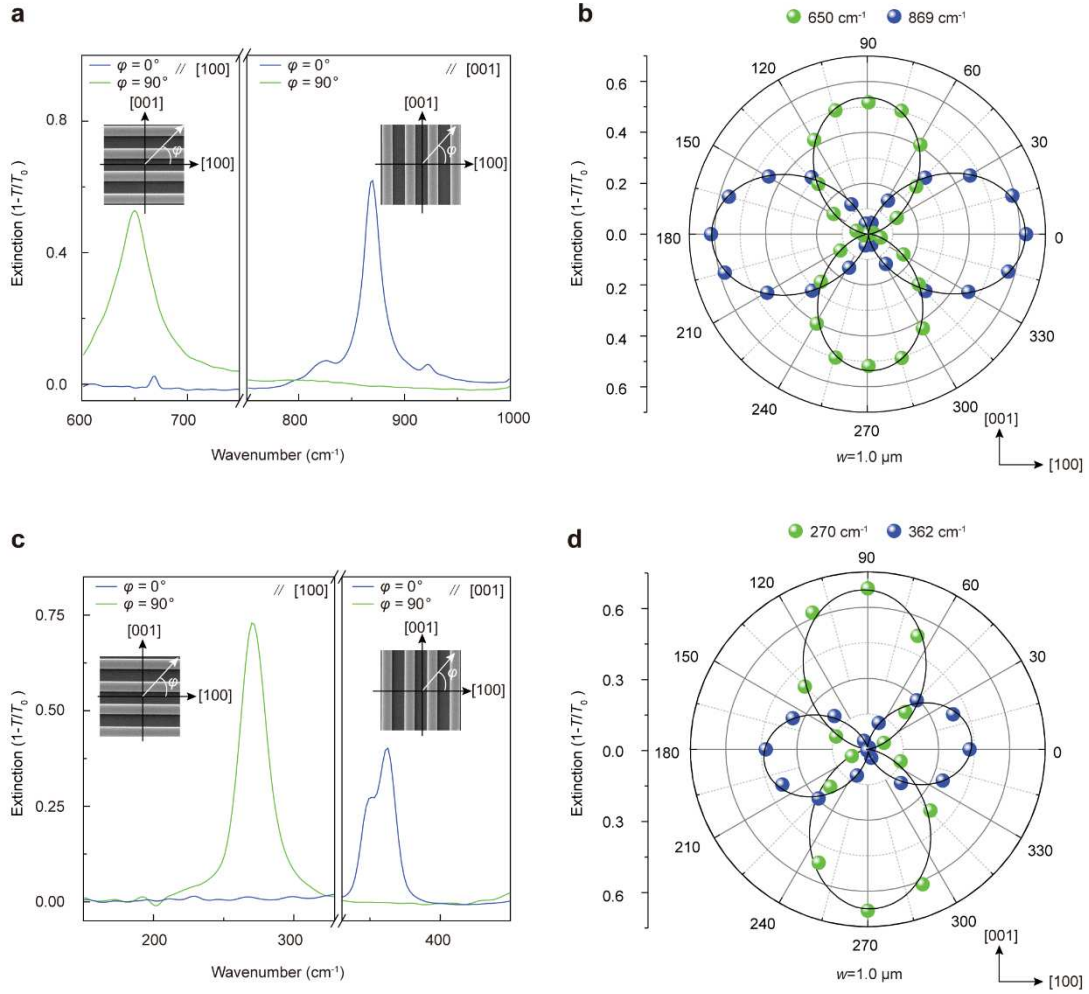


**Fig. 5 | Tunable polarization notch filters in THz and LWIR regimes made up of in-plane hyperbolic polariton tuners.** **a, c,** Polarized extinction spectra of LWIR **(a)** and THz **(c)** notch filters. The long axes of the ribbons are parallel to  $[100]$  (left panels) and  $[001]$  (right panels) crystallographic directions, respectively. The widths of the ribbons are  $1.0 \mu\text{m}$ . Insets: Schematic of the polarization excitation.  $\varphi$  is the angle between incident electric field and  $[100]$  crystallographic direction. The results show that the polariton resonances only appear when the excitation polarization is perpendicular to the ribbon long axis. **b, d,** Polar plots of the extinction as a function of excitation polarization at resonance frequencies of  $650 \text{ cm}^{-1}/869 \text{ cm}^{-1}$  **(c)** and  $270 \text{ cm}^{-1}/362 \text{ cm}^{-1}$  **(d)**. The symbols and solid lines are experimental data and the corresponding fittings using a cosine squared function. The long axes of the ribbons are parallel to  $[100]$  (corresponding to resonances at  $650$  and  $270 \text{ cm}^{-1}$ ) and  $[001]$  (corresponding to resonances at  $869$  and  $362 \text{ cm}^{-1}$ ) crystallographic directions, respectively.

## Conclusions and prospects

The in-plane hyperbolic polariton tuner we propose in this study is proved to be a novel device with unique set of functions. We have successfully demonstrated direct far-field excitation and characterization of resultant effects at far-field of tuning LWIR and THz HPhPs in biaxial vdW  $\alpha\text{-MoO}_3$  with simple patterned surface. The resultant characteristic functions at far-field include tunable polarization, with polarization extinction ratios up to 6.5 dB, high Q-factors up to 300, and selection of desired

wavelength of reflection and transmission, as well as regulation of output light intensity. Such a compositional set of output characteristics observed at far-field is given rise to with a single device and that is unique. They are strongly dependent upon not only the in-plane hyperbolic polariton, but also the excitation polarization and the orientation and structure of patterns.

On the prospects, the findings of this study have important practical applications and implications for fundamental research. From the application point of view, an in-plane hyperbolic polariton tuner, such as that fabricated and demonstrated, is in fact a real single stand device, and can be used in optical circuitry, instruments and even modern information systems. One can desire and produce many other types of devices for various application based on the principle given in this study. Besides, the in-plane hyperbolic polariton tuner opens up new avenues for a variety of practical photonic and optoelectronic applications. For example, by engineering the tuner to spectrally overlap the HPhP resonance with a specific vibration or rotation transition of a molecule, strong interactions between the tuner and molecule can be induced<sup>49,62,63</sup>, which can significantly enhance the molecular absorption or emission and give rise to various ultrasensitive bio-sensing techniques. The tuners with high-Q and tunable HPhP resonances can also be employed to regulate the blackbody emission<sup>61</sup>, whereby narrow-band, polarized, and tunable thermal emission can be achieved<sup>64-67</sup>. Moreover, tunable and high-performance LWIR and THz photodetectors can also be envisioned by taking advantage of the strong light field localizations (Fig. S5 in Supplementary Information) and semiconductor nature of the  $\alpha$ -MoO<sub>3</sub><sup>20</sup>; this type of devices may give unique functions necessary for future communication and radar applications.

For fundamental research, the far-field excitation methodology can complement near-field nano-imaging techniques and make the characterizations of PhPs of materials more precisely, especially for those with in-plane hyperbolicity. For example, in nano-imaging measurement, because the polariton waves are launched by an antenna (the scanning tip or antenna fabricated onto the sample surface), in principle these HPhPs can propagate along different directions determined by the hyperbolic IFC<sup>9-11</sup>. Therefore, the measurements of the polariton wavelength and dispersion relation from the polariton interference fringes can be disturbed by these various polariton waves. On the other hand, with far-field excitation, the polariton wavevector is determined by the tuner's structural parameter and orientation. For a specific pattern only one HPhP mode can be excited, which allows for more accurate characterization of the intrinsic HPhP properties. Additionally, it is possible to characterize the HPhPs using a broadband light source covering a broad THz spectral range. This can unveil more complete polaritonic properties for broadening and deepening our understanding of the THz HPhPs, in particular of new materials such as two-dimensional atomic crystals (*e.g.*, the in-plane IFCs in THz domain as shown in Fig. S8 in Supplementary Information), which is now limited by the discrete laser lines used in most nano-imaging measurements<sup>33</sup>.

It is noted that in the current study, as a demonstration of principle, we only employ the simplest form of patterns, and only demonstrate with one type of material. In fact, patterns can be chosen depending on desirable applications, and also materials as long as supporting HPhPs in the THz and LWIR regimes<sup>7,68</sup>. The tuner allows us to modulate the wavefront of the incident light and control their power flow in an engineered space<sup>22-29</sup>, which therefore enables a variety of interesting applications, such as negative refraction, beam steering, holography, metalens, polarization conversion, and among others, in visible and near-infrared ranges to be expanded into

the THz and LWIR spectral regimes.

## Methods

**Synthesis of large-area vdW  $\alpha$ -MoO<sub>3</sub> flake.** vdW  $\alpha$ -MoO<sub>3</sub> thin flakes with a centimeter lateral size were prepared using a modified thermal physical vapor deposition method. Specifically, an alumina crucible filled with 0.1-g  $\alpha$ -MoO<sub>3</sub> powders was placed at the center of a quartz tube as the evaporation source. Another crucible covered with a silicon substrate of 1 cm $\times$  1 cm was placed 20-cm away from the source. The source was then heated up to 780 °C and held at that temperature for 2 h. The  $\alpha$ -MoO<sub>3</sub> powders were sublimated and crystallized onto the silicon wafer. Afterwards, the quartz tube was cooled down to room temperature naturally. The large-area  $\alpha$ -MoO<sub>3</sub> flakes can be found on the silicon wafer.

**Fabrication of the vdW  $\alpha$ -MoO<sub>3</sub> 1D periodic tuner patterns.** The as-grown  $\alpha$ -MoO<sub>3</sub> flakes were transferred to a pristine (highly resistive) silicon substrate covered with a 300-nm oxide layer. Afterwards, a selected flake was patterned into 1D-PRPs with different  $w$  and  $\theta$  using a combination of electron beam lithography (EBL: EBPG5000+, Netherlands) and reactive ion etching (RIE: 50 W for 10 min). For the EBL processing a 400-nm layer of Poly(methylmethacrylate) (PMMA) photoresist was used. For the RIE etching, a mixture of O<sub>2</sub> (12 vol.%), Ar (30 vol.%), and CHF<sub>3</sub> (58 vol.%) was employed. The etching was conducted at 50 W for 10 min. To guarantee good signal-to-noise ratios of the spectral characterizations, the areas of the patterns were set as 50  $\mu$ m $\times$  50  $\mu$ m and 300  $\mu$ m $\times$  300  $\mu$ m for LWIR and THz regimes, respectively.

**Reflectance and transmittance spectral characterizations.** LWIR and THz spectral characterizations were performed using a Bruker FTIR spectrometer (Vertex 70v) integrated with a Hyperion 3000 microscope and a mercury cadmium telluride (HgCdTe) photoconductor (for the measurement of LWIR spectra) or a liquid-helium-cooled silicon bolometer (or the measurements of THz spectra) as the detector. A broadband black-body light source covering the LWIR and THz spectral regimes was employed as the incident light. A 15 $\times$  reflective Schwarzschild objective was utilized to focus the incident light onto the tuner patterns with a spot size of  $\sim$  500  $\mu$ m. The reflected or transmitted light were collected from an area of 50  $\mu$ m $\times$  50  $\mu$ m and 300  $\mu$ m $\times$  300  $\mu$ m for LWIR and THz regimes, respectively, with the help of an iris diaphragm. For the polarization-dependent measurements, a polarizer was used to control the polarization of the incident light. For the reflectance and transmittance spectra of the tuner, a bare silicon substrate is used as reference for normalization. To characterize the PNFs in LWIR and THz regimes, a linear polarizer was placed before the detector to determine the polarization state of light transmitting through the tuners upon an unpolarized illumination.

## Acknowledgements

H.C. and S.D. acknowledge support from the National Key Basic Research Program of China (grant nos. 2019YFA0210200 and 2019YFA0210203), H.C. acknowledges supports from the National Natural Science Foundation of China (grant no. 91963205), the Guangdong Basic and Applied Basic Research Foundation (grant no. 2020A1515011329), and the Changjiang Young Scholar Program. Z.Z. acknowledges the supports from the National Natural Science Foundation of China (grant no. 11904420), the Guangdong Basic and Applied Basic Research Foundation (grant no.

2019A1515011355), and the project funded by China Postdoctoral Science Foundation (grant no. 2019M663199). J.D.C. acknowledges support from NSF #2128240. T.G.F acknowledges support from University of Iowa startup funding.

### Author contributions

H.C., S.D., N.X, and J.D.C. conceived and designed the experiments. W.H. fabricated the tuner patterns, characterized the far-field spectra, and analyzed the data. T.G.F., Q.X., Z.Z. participated in the far-field spectroscopy measurements. T.G.F., H.Y., and Q.X. measured the THz spectra. F.S. and Z.Z. conducted the numerical simulations and theoretical calculations. J.J. helped fabricate the tuner patterns. H.C., S.D., N.X., J.D.C., and H.Y. coordinated and supervised the work and discussed and interpreted the results. H.C. and W.H. co-wrote the manuscript with the input of all other co-authors. W.H., T.G.F., F.S, and Z.Z. contributed equally to the work.

### Competing interests

The authors declare no competing interests.

### Additional information

Supplementary information is available for this paper at xxx.

### References

1. Caldwell, J. D. *et al.* Atomic-scale photonic hybrids for mid-infrared and terahertz nanophotonics. *Nat. Nanotechnol.* **11**, 9–15 (2016).
2. Koppens, F. H. L. *et al.* Photodetectors based on graphene, other two-dimensional materials and hybrid systems. *Nat. Nanotechnol.* **9**, 780–193 (2014).
3. Guo, Q. S. *et al.* Efficient electrical detection of mid-infrared graphene plasmons at room temperature. *Nat. Mater.* **17**, 986–993 (2018).
4. Cai, X. *et al.* Sensitive room-temperature terahertz detection via the photothermoelectric effect in graphene. *Nat. Nanotechnol.* **9**, 814–819 (2014).
5. Dai, S. Y. *et al.* Tunable phonon polaritons in atomically thin van der Waals crystals of boron nitride. *Science* **343**, 865–871 (2014).
6. Sengupta, K., Nagatsuma, T. & Mittleman, D. M. Terahertz integrated electronic and hybrid electronic–photonic systems. *Nat. Electron.* **1**, 622–635 (2018).
7. Passler, N. C. *et al.* Hyperbolic shear polaritons in low-symmetry crystals. *Nature* **602**, 595–600 (2022).
8. Caldwell, J. D. *et al.* Sub-diffractive volume-confined polaritons in the natural hyperbolic material hexagonal boron nitride. *Nat. Commun.* **5**, 5221 (2014).
9. Zheng, Z. *et al.* Highly confined and tunable hyperbolic phonon polaritons in van der Waals semiconducting transition metal oxides. *Adv. Mater.* **30**, 1705318 (2018).
10. Ma, W. *et al.* In-plane anisotropic and ultra-low-loss polaritons in a natural van der Waals crystal. *Nature* **562**, 557–561 (2018).
11. Zheng, Z. *et al.* A mid-infrared biaxial hyperbolic van der Waals crystal. *Sci. Adv.* **5**, eaav8690 (2019).
12. Dang, S. *et al.* What should 6G be? *Nat. Electron.* **3**, 20–29 (2020).
13. Sengupta, K., Nagatsuma, T. & Mittleman, D. M. Terahertz integrated electronic and hybrid electronic–photonic systems. *Nat. Electron.* **1**, 622–635 (2018).
14. Gade, R. & Moeslund, T. B. Thermal cameras and applications: a survey. *Mach. Vision Appl.* **25**, 245–262 (2014).
15. Lahiri, B. B. *et al.* Medical applications of infrared thermography: a review. *Infrared Phys. Technol.* **55**, 221–235 (2012).

16. Dhillon, S. S. *et al.* The 2017 terahertz science and technology roadmap. *J. Phys. D.: Appl. Phys.* **50**, 043001 (2017).
17. Baranov, D. G. *et al.* Nanophotonic engineering of far-field thermal emitters. *Nat. Mater.* **18**, 920–930 (2019).
18. The Event Horizon Telescope Collaboration *et al.* First M87 event horizon telescope results. I. The shadow of the supermassive black hole. *Astrophys. J.* **875**, L1 (2019).
19. Kopytko, M. & Rogalski, A. Figure of merit for infrared detector materials. *Infrared Phys. Technol.* **122**, 104063 (2022).
20. Gubbin, C. R., Liberato, S. D. & Folland, T. G. Surface phonon polaritons for infrared optoelectronics. *J. Appl. Phys.* **131**, 030901 (2022).
21. Rogalski, A. *et al.* Trends in performance limits of the hot infrared photodetectors. *Appl. Sci.* **11**, 501 (2021).
22. Kildishev, A. V., Boltasseva, A. & Shalaev, V. M. Planar photonics with metasurfaces. *Science* **339**, 1232009 (2013).
23. Cui, T. J. *et al.* Coding metamaterials, digital metamaterials and programmable metamaterials. *Light Sci. Appl.* **3**, e218 (2014).
24. Jahani, S. & Jacob, Z. All-dielectric metamaterials. *Nat. Nanotechnol.* **11**, 23–36 (2016).
25. Watts, C.M. *et al.* Terahertz compressive imaging with metamaterial spatial light modulators. *Nat. Photonics* **8**, 605–609 (2009).
26. Herrmann, E. *et al.* Modulators for mid-infrared and terahertz light. *J. Appl. Phys.* **128**, 140903 (2020).
27. Belacel, C. *et al.* Optomechanical terahertz detection with single meta-atom resonator. *Nat. Commun.* **8**, 1578 (2018).
28. Wei, J. *et al.* Mid-infrared semimetal polarization detectors with configurable polarity transition. *Nat. Photonics* **15**, 614–621 (2021).
29. He, M. Z. *et al.* Deterministic inverse design of Tamm plasmon thermal emitters with multi-resonant control. *Nat. Mater.* **20**, 1663–1669 (2021).
30. Tassin, P. *et al.* A comparison of graphene, superconductors and metals as conductors for metamaterials and plasmonics. *Nat. Photonics* **6**, 259–264 (2012).
31. Taboada-Gutiérrez, J. *et al.* Broad spectral tuning of ultra-low-loss polaritons in a van der Waals crystal by intercalation. *Nat. Mater.* **19**, 964–968 (2020).
32. Caldwell J. D. *et al.* Low-loss, infrared and terahertz nanophotonics using surface phonon polaritons. *Nanophotonics* **4**, 44–68 (2015).
33. De Oliveira, T. V. A. G. *et al.* Nanoscale-confined terahertz polaritons in a van der Waals crystal. *Adv. Mater.* **33**, 2005777 (2021).
34. Zheng, Z. *et al.* Controlling and focusing in-plane hyperbolic phonon polaritons in  $\alpha$ -MoO<sub>3</sub> with a curved plasmonic antenna. *Adv. Mater.* **34**, 2104164 (2022).
35. Hu, G. *et al.* Topological polaritons and photonic magic angles in twisted  $\alpha$ -MoO<sub>3</sub> bilayers. *Nature* **582**, 209–213 (2020).
36. Zheng, Z. *et al.* Phonon polaritons in twisted double-layers of hyperbolic van der Waals crystals. *Nano Lett.* **20**, 5301–5308 (2020).
37. Duan, J. *et al.* Twisted nano-optics: manipulating light at the nanoscale with twisted phonon polaritonic slabs. *Nano Lett.* **20**, 5323–5329 (2020).
38. Chen, M. *et al.* Configurable phonon polaritons in twisted  $\alpha$ -MoO<sub>3</sub>. *Nat. Mater.* **19**, 1307–1311 (2020).
39. Álvarez-Pérez, G. *et al.* Infrared permittivity of the biaxial van der Waals semiconducting  $\alpha$ -MoO<sub>3</sub> from near- and far-field correlative studies. *Adv. Mater.* **32**, 1908176 (2020).

40. Dai, Z. *et al.* Edge-oriented and steerable hyperbolic polaritons in anisotropic van der Waals nanocavities. *Nat. Commun.* **11**, 6086 (2020).
41. Martín-Sánchez J. *et al.* Focusing of in-plane hyperbolic polaritons in van der Waals crystals with tailored infrared nanoantennas. *Sci. Adv.* **7**, eabj0127 (2021).
42. Huang, W. *et al.* Van der Waals phonon polariton microstructures for configurable infrared electromagnetic field localizations. *Adv. Sci.* **8**, 2004872 (2021).
43. Duan, J. *et al.* Planar refraction and lensing of highly confined polaritons in anisotropic media. *Nat. Commun.* **12**, 4325 (2021).
44. He, M. Z. *et al.* Anisotropy and modal hybridization in infrared nanophotonics using low-symmetry materials. *ACS Photonics* **9**, 1078–1095 (2022).
45. Ju, L. *et al.* Graphene plasmonics for tunable terahertz metamaterials. *Nat. Nanotechnol.* **6**, 630–634 (2011).
46. Yan, H. *et al.* Damping pathways of mid-infrared plasmons in graphene nanostructures. *Nat. Photonics* **7**, 394–399 (2013).
47. Brar, V. W. *et al.* Hybrid surface-phonon-plasmon polariton modes in graphene/monolayer h-BN heterostructures. *Nano Lett.* **14**, 3876–3880 (2014).
48. Alfaro-Mozaz, F. J. *et al.* Deeply subwavelength phonon-polaritonic crystal made of a van der Waals material. *Nat. Commun.* **10**, 42 (2019).
49. Autore, M. *et al.* Boron nitride nanoresonators for phonon-enhanced molecular vibrational spectroscopy at the strong coupling limit. *Light Sci. Appl.* **7**, e17172 (2018).
50. Wang, C. *et al.* Van der Waals thin films of WTe<sub>2</sub> for natural hyperbolic plasmonic surfaces. *Nat. Commun.* **11**, 1158 (2020).
51. Di Pietro, P. *et al.* Observation of Dirac plasmons in a topological insulator. *Nat. Nanotechnol.* **8**, 556–560 (2013).
52. Yang, X. *et al.* Far-field spectroscopy and near-field optical imaging of coupled plasmon–phonon polaritons in 2D van der Waals heterostructures. *Adv. Mater.* **28**, 2931–2938 (2016).
53. Nolen, J. R. *et al.* Ultraviolet to far-infrared dielectric function of n-doped cadmium oxide thin films. *Phys. Rev. Mater.* **4**, 025202 (2020).
54. Berreman, D. W. Infrared absorption at longitudinal optical frequency in cubic crystal films. *Phys. Rev.* **130**, 2193–2198 (1963).
55. Vassant, S. *et al.* Berreman mode and epsilon near zero mode. *Opt. Express* **20**, 23971–23977 (2012).
56. Passler, N. C. *et al.* Second harmonic generation from phononic epsilon-near-zero Berreman modes in ultrathin polar crystal films. *ACS Photonics* **6**, 1365–1371 (2019).
57. Giles, A. J. *et al.* Imaging of anomalous internal reflections of hyperbolic phonon-polaritons in hexagonal boron nitride. *Nano Lett.* **16**, 3858–3865 (2016).
58. Sun, F. *et al.* Polariton waveguide modes in two-dimensional van der Waals crystals: an analytical model and correlative nano-imaging. *Nanoscale* **13**, 4845–4854 (2021).
59. Gao, W. *et al.* Excitation of plasmonic waves in graphene by guided-mode resonances. *ACS Nano* **6**, 7806–7813 (2012).
60. Tamagnone, M. *et al.* High quality factor polariton resonators using van der Waals Materials. <https://arxiv.org/ftp/arxiv/papers/1905/1905.02177.pdf>. (2019).
61. Folland, T. G. & Caldwell, J. D. Precise control of infrared polarization. *Nature* **562**, 499–501 (2018).
62. Yoo, D. *et al.* Ultrastrong plasmon–phonon coupling via epsilon-near-zero nanocavities. *Nat. Photonics* **15**, 125–130 (2021).
63. Yoo, D. *et al.* High-contrast infrared absorption spectroscopy via mass-produced

- coaxial zero-mode resonators with sub-10 nm gaps. *Nano Lett.* **18**, 1930–1936 (2018).
64. Wang, T. *et al.* Phonon-polaritonic bowtie nanoantennas: controlling infrared thermal radiation at the nanoscale. *ACS Photonics* **4**, 1753–1760 (2017).
65. Lu, G. Y. *et al.* Collective phonon–polaritonic modes in silicon carbide subarrays. *ACS Nano* **16**, 963–973 (2022).
66. Lu, G. Y. *et al.* Multi-frequency coherent emission from superstructure thermal emitters. *Appl. Phys. Lett.* **118**, 141102 (2021).
67. Schuller J. A., Taubner, T. & Brongersma, M. L. Optical antenna thermal emitters. *Nat. Photonics* **3**, 658–661 (2009).
68. Ma, W. L. *et al.* Ghost hyperbolic surface polaritons in bulk anisotropic crystals. *Nature* **596**, 362–366 (2021).

## Supplementary Files

This is a list of supplementary files associated with this preprint. Click to download.

- [vdWMoO3nanogratingNCommunSlv1.doc](#)